J Supercond Nov Magn
DOI 10.1007/s10948-015-3009-6

ORIGINAL PAPER

Magnetic Properties of Dysprosium-Doped Cobalt Ferrite Nanoparticles Synthesized by Starch-Assisted Sol-Gel Auto-combustion Method

Raghvendra Singh Yadav · Jaromir Havlica · Ivo Kuřitka · Zuzana Kozakova · Martin Palou · Eva Bartoníčková · Martin Boháč · Františka Frajkorová · Jiri Masilko · Lukas Kalina · Miroslava Hajdúchová · Vojtěch Enev · Jaromir Wasserbauer

Received: 26 December 2014 / Accepted: 24 January 2015

Abstract Dysprosium-substituted cobalt ferrite nanoparticles with composition of $CoFe_{2-x}Dy_xO_4$ ($x = 0 - 0.1$ in a step of 0.025) were synthesized by starch-assisted sol–gel auto-combustion method. The effect of Dy^{3+} cation substitution on structural and magnetic properties of cobalt ferrite nanoparticles was investigated. Powder X-ray diffraction (XRD), field-emission scanning electron microscopy (FE-SEM), Raman spectroscopy, infrared spectroscopy (IR), X-ray photoelectron spectroscopy and vibrating sample magnetometer (VSM) were employed to characterize the physical properties of these ferrite nanoparticles. XRD pattern reveals the formation of cubic spinel ferrite with the signature of $DyFeO_3$ phases for $x \geq 0.05$. An infrared spectroscopy study shows the presence of two absorption bands in the frequency range around 560 cm^{-1} (ν_1) and around 380 cm^{-1} (ν_2), which indicate the presence of tetrahedral and octahedral group complexes, respectively, within the spinel ferrite nanoparticles. FE-SEM analysis indicated the formation of nanosized particles (5−15 nm) with spherical morphology. Vibrating sample magnetometer was employed to probe the magnetic properties of the samples at room temperature. It was observed that rare earth ion dopant, crystallite size and foreign phase $DyFeO_3$ affect the magnetic properties of cobalt ferrite nanoparticles.

R. S. Yadav (✉) · J. Havlica · M. Palou · E. Bartoníčková · M. Boháč · F. Frajkorová · J. Masilko · L. Kalina · M. Hajdúchová · V. Enev · J. Wasserbauer
Materials Research Centre, Brno University of Technology, Purkyňova 464/118, 61200 Brno, Czech Republic
e-mail: yadav@fch.vutbr.cz

I. Kuřitka · Z. Kozakova
Centre of Polymer Systems, University Institute, Tomas Bata University in Zlin, Nad Ovčírnou 3685, 760 01 Zlín, Czech Republic

Keywords Nanoparticles · Magnetic properties · Spinel ferrites

1 Introduction

Nowadays, magnetic nanoparticles have got considerable attention of the researchers due to their potential applications in the field of high-density magnetic recording, microwave devices and medical sciences [1–4]. Among the magnetic materials, cobalt ferrite ($CoFe_2O_4$) has drawn considerable attention due to remarkable properties, such as high coercivity, moderate saturation magnetization along with good mechanical hardness and chemical stability [5]. The spinel cobalt ferrite material has a tunable magnetic property, and it can be tuned by replacing the A and/or B site with different rare earth ions. The rare earth ions possess a wide variety of magnetic properties as their magnetic moments vary from 0 (La^{3+}) to 10.5 μ_B (Dy^{3+}) [6–10]. One can expect an appearance of spin coupling of $3d$-$4f$ electrons by substitution of small amount of rare earth cations (i.e. the $4f$ elements series) in place of Fe ions. Therefore, the magnetic properties, i.e. saturation magnetization, magnetocrystalline anisotropy constant and magnetic coercivity of nanoparticles can be modified further by substitution of rare earth ions [11].

In reported literature, various synthesis techniques, viz., sol–gel, hydrothermal process, forced hydrolysis method, coprecipitation, ball milling, sonochemical, reverse micelles, solution combustion and microemulsion methods are reported for nanosized ferrite particles [12–15]. Among the various synthesis methods, the auto-combustion method, a wet chemical synthesis method, has numerous advantages owing to low external energy consumption, inexpensive precursors and simpler equipment requirement coupled with

Published online: 13 February 2015

resulting powders being structured, homogeneous and relatively pure. Z. Karimi et al. [21] reported the magnetic property of nanosized Dy-doped cobalt ferrite synthesized by coprecipitation method. The hysteresis loop of the material was affected noticeably by doped elements as the room temperature saturation magnetization was decreased, but the residual magnetization and coercivity of ferrite were promoted after adding dysprosium. Rahul C. Kambale et al. [22] studied the effect of Dy^{3+} content on the magnetic properties of cobalt ferrite single crystal. The single crystals of $CoFe_{1.9}Dy_{0.1}O_4$ were grown by the flux method using $Na_2B_4O_7.10\ H_2O$ (borax) as a solvent (flux). The magnetostriction measurement revealed that the magnetostrictive hysteresis decreased with increase in temperature. The observed saturation magnetization (M_s) and coercivity (H_c) were found to be lower than that of pure $CoFe_2O_4$ single crystal. The magnetic measurements concluded that the single crystals could be used for magneto-optic recording media. R. C. Kambale et al. [23] reported magnetic properties of nanocrystalline Dy^{3+}-doped cobalt ferrite synthesized by glycine-assisted solution combustion method. This research group observed that saturation magnetization and coercivity decreases with Dy^{3+} addition and further proposed that these materials might be applicable for magnetic data storage and recording media.

In this paper, we report the synthesis of $CoFe_{2-x}Dy_xO_4$ (where $x = 0.0$, 0.025, 0.05, 0.075 and 0.1) nanoparticles by starch-assisted sol–gel auto-combustion method. To the best of the authors' knowledge, there are no reports available in the literature regarding to the use of starch in sol–gel auto-combustion synthesis of Dy^{3+} ion doped cobalt spinel ferrite nanoparticles. In this present study, we are utilizing starch from potato, a bio-polymer, as a fuel in sol–gel auto-combustion synthesis of Dy^{3+}-doped cobalt ferrite nanoparticles. We have directed our attention mainly towards the effect of Dy^{3+} on the structural and magnetic properties of $CoFe_2O_4$ nanoparticles synthesized by starch-assisted sol–gel auto-combustion method.

2 Experimental Section

2.1 Materials

All chemicals used in this study were of analytical grade and were used without any further purification. Cobalt (II) nitrate hexahydrate ($Co(NO_3)_2\cdot 6H_2O$), dysprosium (III) nitrate pentahydrate ($Dy(NO_3)_3\cdot 5H_2O$) and iron(III) nitrate nonahydrate ($Fe(NO_3)_3\cdot 9H_2O$) were purchased from Alfa Aesar GmbH & Co KG, Germany. Starch soluble $(C_6H_{10}O_5)_n$ (from potatoes) was purchased from Lach-Ner, Czech Republic.

2.2 Synthesis of Ferrites

In this study, $CoFe_{2-x}Dy_xO_4$ ($x = 0.0$, 0.025, 0.05, 0.075, 0.10) were synthesized by the starch-assisted sol–gel auto-combustion method. In a typical experiment, stoichiometric amount of cobalt nitrate ($Co(NO_3)_2\cdot 6H_2O$), iron nitrate ($Fe(NO_3)_3\cdot 9H_2O$) and dysprosium nitrate ($Dy(NO_3)_3\cdot 5H_2O$) were dissolved in distilled water to obtain a mixed solution. The molar ratio of cobalt nitrate to iron nitrate and dysprosium nitrate was 1:2. The metal nitrates were dissolved together in the minimum amount of double-distilled water needed to obtain a clear solution. An aqueous solution of starch $(C_6H_{10}O_5)_n$ (from potatoes) was mixed with the metal nitrate solution. The mixed solution was placed on a hot plate with continuous stirring at 100 °C. During evaporation, the solution formed a very viscous brown gel. When all of the water molecules were removed from the mixture, the viscous gel began to froth. These as-prepared precursors were annealed in a furnace at 700 °C for 2 h.

2.3 Characterizations

The structural phases of the synthesized dysprosium-doped spinel cobalt ferrite nanoparticles were identified by powder X-ray diffraction recorded using PANalytical Empyrean X-ray diffractometer with CuKα radiation (1.5406 Å). Raman spectra of synthesized ferrite nanoparticles were measured using a confocal microscope with spectrometer "Nanofinder-S" (SOLAR TII, Ltd.). FTIR spectra of synthesized ferrite nanoparticles were recorded using Nicolet iS 50 FTIR spectrometer by the ATR method. The particle size and morphology of the ferrite nanoparticles was inspected using (FEG-SEM) type field emission gun Scanning Electron Microscope Model-JEOL JSM-7600F. Information about the presence of Co^{2+} at the octahedral and tetrahedral sites was confirmed through X-ray photoelectron spectroscopy (XPS) using Kratos Analytical Axis Ultra DLD. The change in magnetic properties with dysprosium ions in cobalt ferrite nanoparticles were measured on a VSM 7407 vibrating sample magnetometer (Lake Shore) at room temperature in air atmosphere.

3 Result and Discussion

3.1 X-ray Diffraction Spectroscopy

The XRD results of $CoFe_{2-x}Dy_xO_4$ ($x = 0.0$, 0.025, 0.05. 0.075. 0.10) nanoparticles, shown in Fig. 1, indicate that the major reflection peaks correspond to the cubic spinel cobalt ferrite (JCPDS card no.22-1086). The apparent broadening of the reflection peaks in XRD patterns confirms that the

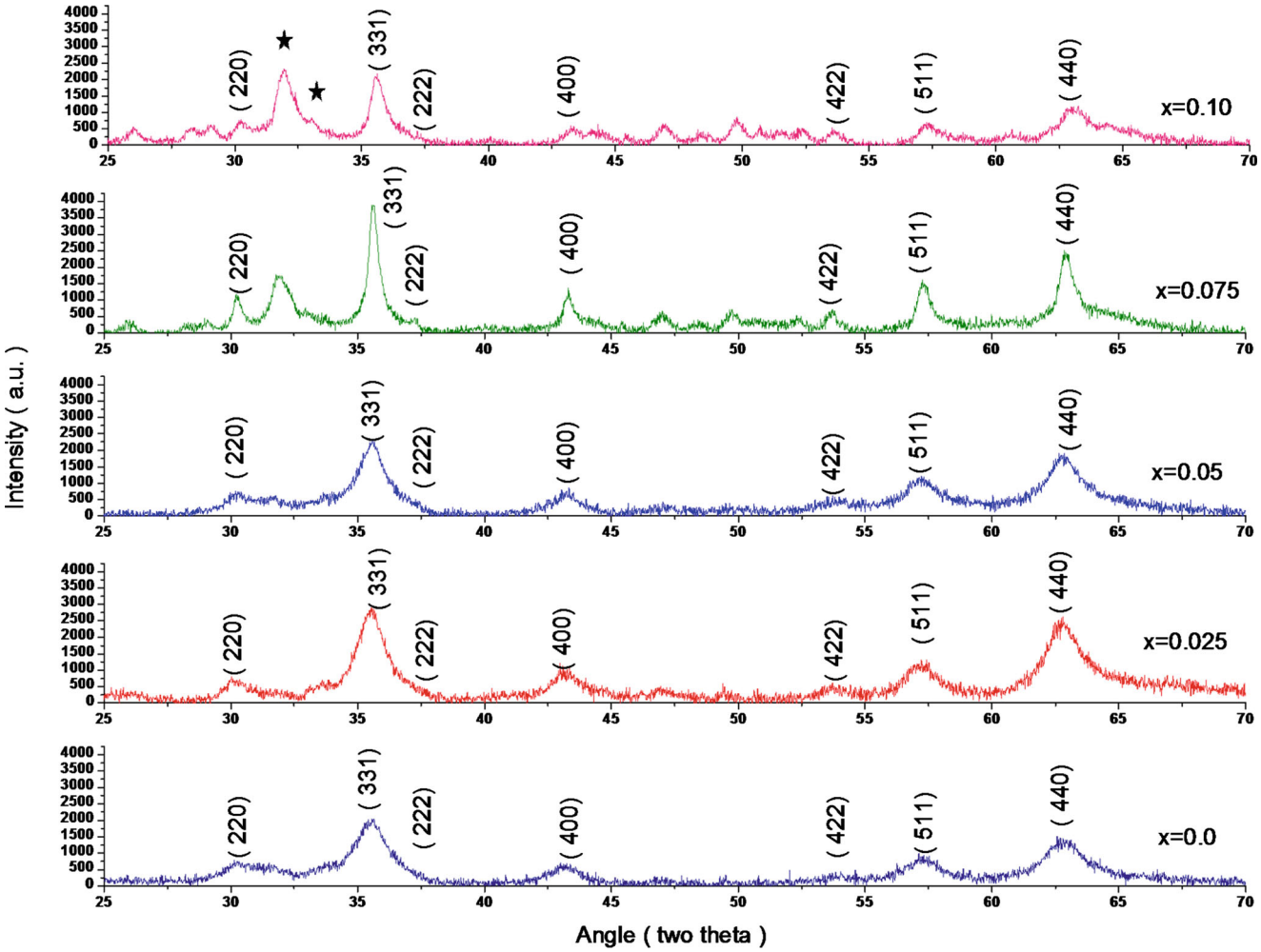

Fig. 1 X-ray diffraction pattern of $CoFe_{2-x}Dy_xO_4$ ($x = 0.0, 0.025, 0.05, 0.075, 0.1$) nanoparticles synthesized by starch-assisted sol–gel auto-combustion method

as-synthesized ferrite particles are of nanocrystalline nature. It is observed that the widths of diffraction peaks became relatively narrower, and the intensities increased with the increase in dopant amount. It indicates that the growth of cobalt ferrite nanoparticles is influenced by amount of dysprosium ions. It is also noticeable that as Dy^{3+} substitution increases the deviation from single phase and becomes more prominent with the appearance of some un-indexed peak as secondary phase. In the synthesized cobalt ferrite, the formation of secondary phases by sol–gel auto-combustion method is governed by the amount of Dy^{3+} used. In reported literature, this is probably due to orthoferrite ($DyFeO_3$) phase [20]. The doping of rare earth (RE) into the spinel lattice suffers the phase segregation and diffusion of the RE species to the grain boundaries even for very low content, causing the precipitation of extra amorphous or crystalline phases like orthoferrites ($REFeO_3$) [21–24], hematite (α-Fe_2O_3) [25, 26] and metal monoxides [27]. The ionic radius of Dy^{3+} ions is 1.05 Å which is larger than that of Fe^{3+} (0.67 Å), and the amount of Fe^{3+} ions substituted by Dy^{3+} ions is limited; therefore, redundant Dy^{3+} ions aggregate on the grain boundaries with formation of $DyFeO_3$ phase. The lattice parameters, strain and average particle size of $CoFe_{2-x}Dy_xO_4$ nanoparticles synthesized by starch-assisted sol–gel auto-combustion method are calculated and listed in Table 1. The lattice parameter of $CoFe_{2-x}Dy_xO_4$ nanoparticles were calculated using the following equation [28]:

$$a = d_{hkl}\sqrt{h^2 + k^2 + l^2}$$

where d is the interplanar distance, a is the lattice parameter and (hkl) are Miller indices.

The lattice constant a gradually increases from 8.373 to 8.383 Å with increasing Dy^{3+} content in cobalt ferrite nanoparticles; therefore, it follow Vegard's law. This linear increase in lattice constant may be attributed to the

Table 1 Crystallite size (nm), lattice parameter (Å), M_s (emu/g), M_r (emu/g), H_c (Oe), K (erg/g) and η_B (μ_B), M_r/M_s value of the $CoFe_{2-x}Dy_xO_4$ ($x = 0.0, 0.025, 0.05, 0.075, 0.1$) nanoparticles synthesized by starch-assisted sol–gel auto-combustion method

x	Crystallite size (nm)	Lattice parameter (Å)	M_s (emu/g)	M_r (emu/g)	H_c (Oe)	$K \times 10^3$ (erg/g)	η_B (μ_B),	M_r/M_s
0.0	4.15	8.373	13.98	0.53	52.38	0.762	0.587	0.037
0.025	4.58	8.374	12.05	0.24	21.29	0.267	0.512	0.019
0.050	4.72	8.375	13.47	0.62	35.10	0.492	0.578	0.046
0.075	12.95	8.381	13.02	3.35	312.84	4.242	0.566	0.257
0.10	11.50	8.383	9.66	1.67	103.46	1.041	0.424	0.173

replacement of smaller Co^{2+} (0.78 Å) and Fe^{3+} (0.64 Å) ions by the larger Dy^{3+} (1.05 Å) ions in the spinel cobalt ferrite nanoparticles. The crystallite size of the dysprosium-doped cobalt ferrite nanoparticles is estimated from the full width at half maximum (FWHM) of the strongest diffraction peak using the Scherrer formula [29]:

$$D = k\lambda/\beta \mathrm{Cos}\theta$$

where D is the crystallite size and k is the shape function. β is the full width at half maximum (FWHM) of the (440) peak, λ is the X-ray wavelength and θ is the diffraction angle. It is observed that with the increase of dysprosium amount (x), the average crystallite size of dysprosium-doped cobalt ferrite nanoparticles increases in the following order: 4.15 nm ($x = 0.0$), 4.58 nm ($x = 0.025$), 4.72 nm ($x = 0.05$), 12.95 nm ($x = 0.075$) and 11.50 nm ($x = 0.10$), as shown in Table 1.

3.2 Raman Spectroscopy

Cobalt ferrite has a cubic inverse ferrite structure with O_h^7 ($Fd\bar{3}m$ space group) which gives rise to 39 normal vibrational modes, out of which five are Raman active, namely A_{1g}, E_g and $3T_{2g}$ [30]. The modes below about 600 cm^{-1} are attributed to vibrations of oxygen within the octahedral site, while vibrations within the tetrahedral sites appear above 600 cm^{-1} [31]. Raman spectroscopy of the spinel ferrite nanoparticles in the region 175–900 cm^{-1} at room temperature is carried out to further characterize the variation of the structure with the doping of Dy^{3+} ions in cobalt ferrites. Figure 2 shows the Raman spectrum of the $CoFe_{2-x}Dy_xO_4$ ($x = 0.0, 0.025, 0.05, 0.075, 0.1$) spinel ferrite nanoparticles synthesized by starch-assisted sol–gel auto-combustion method. The formation of the $CoFe_{2-x}Dy_xO_4$ spinel ferrite structure in the nanocrystalline form was supported by Raman spectra. $CoFe_{2-x}Dy_xO_4$ ($x = 0.0$) nanoparticles show six peak maxima at 185.46, 317.17, 471.64, 524.62, 621.12, and 678.09 cm^{-1}, as mentioned in Table 2, most of which are the typical modes of the cubic inverse-spinel ferrite structure. However, $CoFe_2O_4$ doped with Dy ($x = 0.025$) nanoparticles show six peak maxima at 193.27, 305.38, 470.64, 520.80, 624.94 and 685.90 cm^{-1}. Further, the variation in Raman modes at higher value of Dy dopant, i.e. $x = 0.05$,

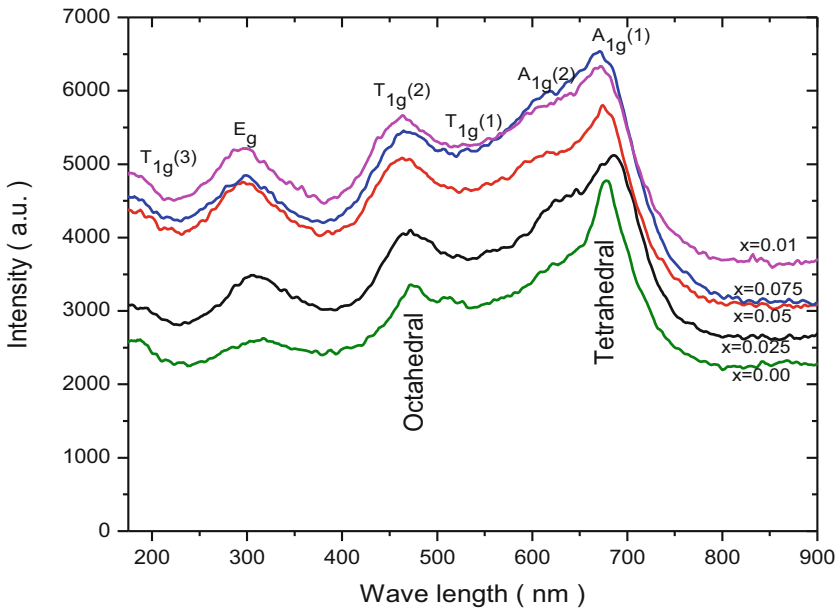

Fig. 2 Raman spectra of $CoFe_{2-x}Dy_xO_4$ ($x = 0.0, 0.025, 0.05, 0.075, 0.1$) nanoparticles synthesized by starch-assisted sol–gel auto-combustion method

Table 2 Raman peaks of the $CoFe_{2-x}Dy_xO_4$ ($x = 0.0, 0.025, 0.05, 0.075, 0.1$) nanoparticles synthesized by starch-assisted sol–gel auto-combustion method

x	Raman peak (cm^{-1})					
	$A_{1g}(1)$	$A_{1g}(2)$	$T_{1g}(1)$	$T_{1g}(2)$	E_g	$T_{1g}(3)$
0.0	678.09	621.12	524.62	471.64	317.17	185.46
0.025	685.90	624.94	520.80	470.64	305.38	193.27
0.05	674.11	616.14	529.61	462.44	295.39	186.29
0.075	671.83	626.67	526.37	462.44	296.38	186.29
0.1	670.01	627.66	527.37	463.63	296.38	187.28

0.075 and 0.10 are also observed as comparison to undoped $CoFe_2O_4$, as listed in Table 2. The variation in Raman modes of $CoFe_{2-x}Dy_xO_4$ ($x = 0.0, 0.025, 0.05, 0.075, 0.1$) nanoparticles synthesized by starch-assisted sol–gel auto-combustion method may be due to the incorporation of dysprosium dopant, change of crystallite size, lattice constant, strain and cation distribution, etc. [32–36]. It may be also considered that with the substitution of large Dy^{3+} ions for Fe^{3+} ions and Co^{2+} ions at the octahedral sites, the difference of Dy–O, Co–O and Fe–O bond length may give rise to the presence of ion vacancies, lattice defect or the loss of symmetry at these sites, which is responsible for the frequency shift for Raman active mode in dysprosium doped cobalt ferrite nanoparticles, as listed in Table 2.

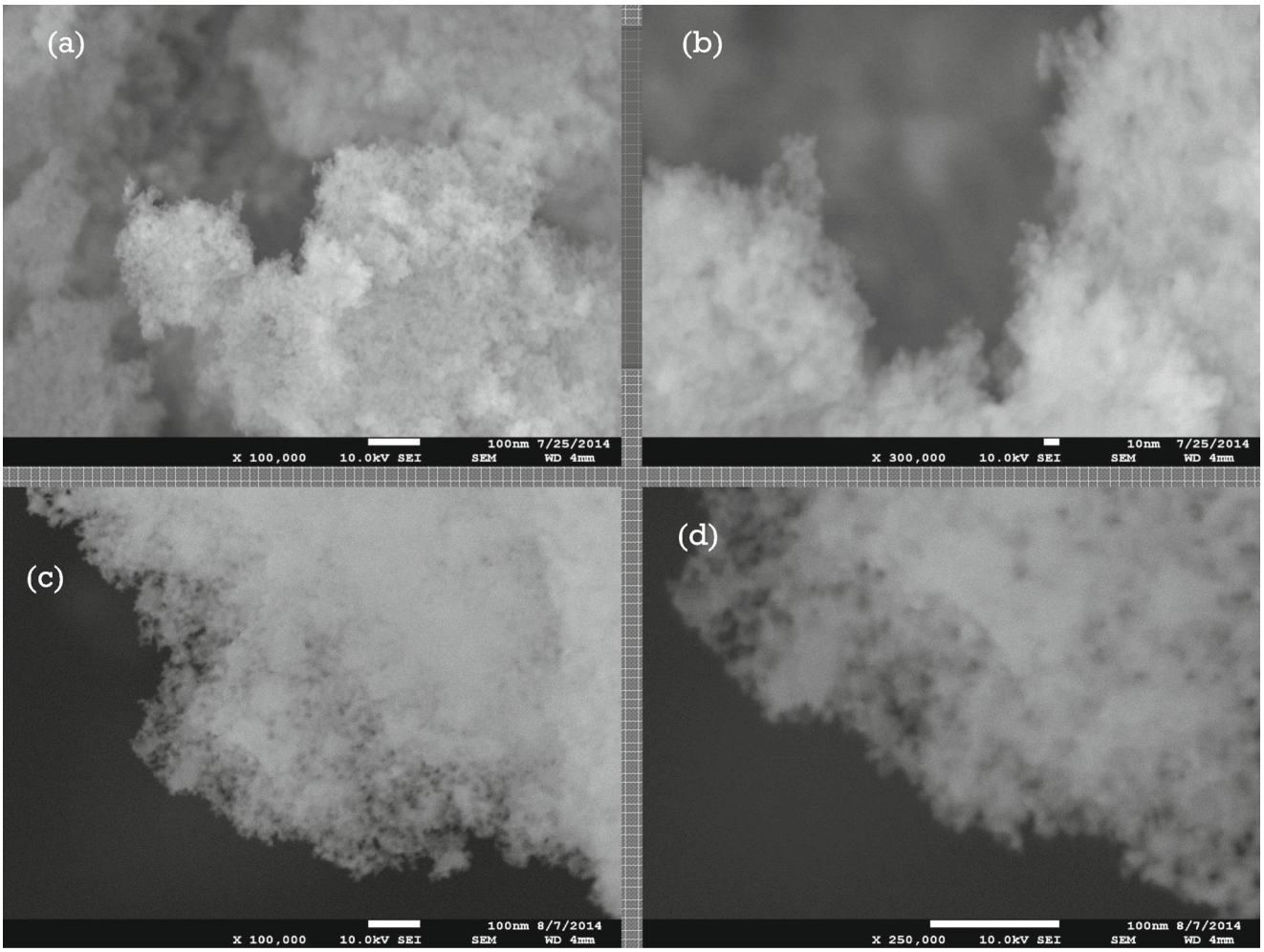

Fig. 3 FE-SEM image of $CoFe_{2-x}Dy_xO_4$ ($x = 0.0$ and 0.075) nanoparticles synthesized by starch-assisted sol–gel auto-combustion method, at **a**, **b** $x = 0.00$, at **c**, **d** $x = 0.075$

3.3 Field Emission Scanning Electron Microscopy

The morphology and particle size of the prepared $CoFe_{2-x}Dy_xO_4$ ($x = 0.0, 0.075$) nanoparticles were studied by using field emission scanning electron microscopy (FE-SEM). Figure 3 shows the FE-SEM micrographs of the samples with composition of $x = 0.0$ and 0.075 in $CoFe_{2-x}Dy_xO_4$ nanoparticles. It is interesting to find that the dysprosium cation substitution had no obvious influence on the morphology, but slightly affected the particle size. The undoped cobalt ferrite nanoparticles were in the range of 5–10 nm with spherical morphology. However, dysprosium cation-doped cobalt ferrite ($x = 0.075$) was in the range of 8–15 nm with spherical morphology. The grain size derived from FE-SEM micrographs is found to be larger than that estimated from XRD data. This indicates that every particle is formed by aggregation of a large number of crystallites or grains.

3.4 Infrared Spectroscopy

In ferrites, the metal ions are situated in two different sublattices designated tetrahedral (A site) and octahedral (B site) according to the geometrical configuration of the oxygen nearest neighbors. R. D. Waldron [37] have attributed the absorption band around 600 cm^{-1} to stretching vibrations of the tetrahedral groups (ν_A) and around 400 cm^{-1} to the octahedral group (ν_B). The Fourier transform infrared spectroscopy (FTIR) of $CoFe_{2-x}Dy_xO_4$ ($x = 0.0, 0.025, 0.05, 0.075, 0.1$) nanoparticles synthesized by starch-assisted sol–gel auto-combustion method were recorded on Nicolet iS 50 spectrometer using ATR method and shown in Fig. 4. It is observed from Fig. 4 that the FTIR spectra of all the sample show two principle absorption bands near 550–570 cm^{-1} (ν_1) and the second absorption band near 380–350 cm^{-1} (ν_2). In the present study, the ν_1 frequency for $CoFe_{2-x}Dy_xO_4$ was 562.46 cm^{-1}($x = 0.0$), 563.05 cm^{-1} ($x = 0.025$), 562.17 cm^{-1}($x = 0.05$), 558.67 cm^{-1}($x = 0.075$) and 556.63 cm^{-1} ($x = 0.10$). The ν_2 frequency for $CoFe_{2-x}Dy_xO_4$ was 356.90 cm^{-1}($x = 0.0$), 364.48 cm^{-1} ($x = 0.025$), 362.73 cm^{-1}($x = 0.05$), 387.52 cm^{-1}($x = 0.075$) and 416.96 cm^{-1} ($x = 0.10$). In reported literature [38–40], the change in ν_1 and ν_2 was attributed to the changes in bond length of oxygen O^{2-} and metal ions Co^{2+} and Fe^{3+} at the octahedral and tetrahedral sites. In the present study, the observed change in frequency position is

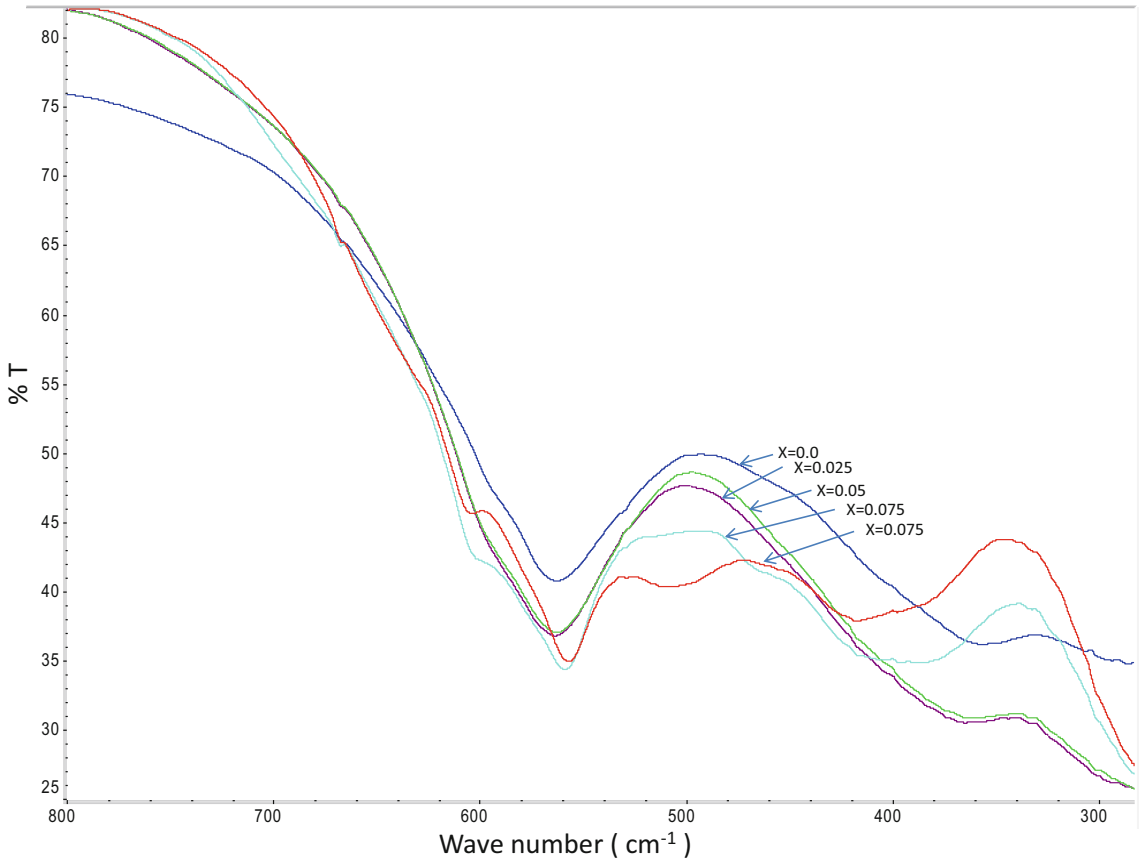

Fig. 4 FTIR spectra of $CoFe_{2-x}Dy_xO_4$ ($x = 0.0, 0.025, 0.05, 0.075, 0.1$) nanoparticles synthesized by starch-assisted sol–gel auto-combustion method

due to entrance of Dy^{3+} ions with larger ionic radius into the octahedral lattice sites (B) of the spinel lattice induces partial migration of Co^{2+} ions from the B site to A one, accompanied by an opposite transfer of an equivalent number of Fe^{3+} ions from the A to B sites in order to relax the strain [41, 42]. It is well known that vibration frequency is proportional to force constant (F); therefore, the band shift of ν_1 and ν_2 frequency with change of Dy^{3+} content indicates that the force constant changes. The calculated values of the force constant F_T and F_B for the A and the B sites, respectively, are listed in Table 3 using the following relation [43]:

$$F = 4\pi^2 c^2 \nu^2 m$$

where F is the force constant, c is the light velocity 2.99×10^{10} cm/s, ν is the vibration frequency of the A and B sites, m is the reduced mass for the Fe^{3+} ions and the O^{2-} ions ($\sim 2.065 times 10^{-23}$g/mol). The peak intensity of frequency bands slightly changes with an increasing Dy^{3+} substitution. It is known that the intensity ratio is a function of the change of dipole moment with the internuclear distance ($d\mu/dr$) [44]. This value represents the contribution of the ionic bond Fe–O in the lattice. Therefore, the observed change in the peak intensity with an increasing Dy^{3+} content is presumably due to the perturbation occurring in Fe–O bonds by substitution the Dy^{3+} ions and redistribution of the Co^{2+} and Fe^{3+} ions at the octahedral and tetrahedral sites. The broadening in ferrites has been commonly observed in the spectral bands. The broadening is due to statistical distribution of cations over the octahedral and tetrahedral sites [45].

3.5 X-ray Photoelectron Spectroscopy

The X-ray photoelectron spectroscopic (XPS) analysis was employed to study the elements and oxidation states of the prepared ferrite $CoFe_{2-x}Dy_xO_4$ ($x = 0.05$) nanoparticles synthesized by starch-assisted sol–gel combustion method, as shown in Fig. 5. The collected XPS spectra of sample were analysed using CasaXPS software (version 2.2.16). All spectra were calibrated using the adventitious C 1s peak with a fixed value of 284.8 eV. A Shirley-type background subtraction was used to fit the curve using a 70 % Gaussian–30 % Lorentzian function. The XPS spectrum, as shown in Fig. 5a, confirms the elements to be present in dysprosium-doped cobalt ferrite nanoparticles. High-resolution XPS spectrum of Co shows satellite peaks that appear on the high binding energy side of both $2p_{3/2}$ and $2p_{1/2}$ regions for the $CoFe_{2-x}Dy_xO_4$ ($x = 0.05$) nanoparticles, as shown in Fig. 5b. This observation of the strong satellite peak indicates that Co is in an oxidation state of +2. Satellite peaks is due to the multiplet splitting for Co in the +2 state [46]. The Co region was further deconvoluted for the octahedral versus tetrahedral peaks and quantitative analyses of the Co^{2+} at these sites in the $CoFe_{2-x}Dy_xO_4$ ($x = 0.05$) nanoparticles. Deconvolution of the $2p_{3/2}$ peak regions exposes the presence of two nonequivalent bonds due to two types of lattice sites, i.e. tetrahedral and octahedral. The binding energies associated with Co $2p_{3/2}$ were 779.9 and 781.9 eV. The binding energy peak 779.9 eV appears since Co^{2+} have the octahedral (O_h) bonding with oxygen, whereas peak 781.9 eV is due to the tetrahedral (T_d) bonding of Co^{2+} with oxygen. The relative contributions to the overall intensity of Co^{2+} ions at the octahedral and tetrahedral sites were 60 and 41 %, respectively. Furthermore, to endorse the presence of Fe^{3+} in the $CoFe_{2-x}Dy_xO_4$ ($x = 0.05$) nanoparticles, the Fe $2p$ XPS spectra were fitted using Gaussian–Lorentzian (GL30) line shapes after subtracting a Shirley-type background, as shown in Fig. 5c. Based on spin-orbital splitting, it consists of Fe $2p_{3/2}$ and Fe $2p_{1/2}$ components and it was at 711.8 and 725.5 eV, respectively. An additional peak exists as satellite peak in between the Fe $2p_{1/2}$ and Fe $2p_{3/2}$. The satellite peak was at 719.4 eV. The difference of 6.1 eV from the satellite peak to Fe $2p_{1/2}$ peak (725.5 eV) was identified as Fe^{3+} state [47]. In Fig. 5c, the Fe $2p_{3/2}$ main peak, shouldering with a satellite peak at 719.4 eV, is fitted into two signals positioned at 710.7 and 713.1 eV; it indicates the existence of Fe species also in two different lattice sites. The binding energy at 710.7 eV arises from Fe^{3+} ions in the octahedral sites, while the binding energy at 713.1 eV is caused by Fe^{3+} ions in the tetrahedral sites [48]. According to the integrated intensity of the fitted doublets, the distribution of Fe^{3+} ions is obtained to be about 69 % in the octahedral sites and about 31 % in the tetrahedral sites.

Table 3 Frequency ν_1 and ν_2 and force constant F_T and F_B for the A and the B sites, respectively, for the $CoFe_{2-x}Dy_xO_4$ ($x = 0.0, 0.025, 0.05, 0.075, 0.1$) nanoparticles synthesized by starch-assisted sol–gel auto-combustion method

x	ν_1(cm^{-1})	ν_2(cm^{-1})	$F_T \times 10^5$(dyne/cm^2)	$F_B \times 10^5$(dyne/cm^2)
0.0	562.46	356.90	2.303	0.927
0.025	563.05	364.48	2.308	0.967
0.05	562.17	362.73	2.301	0.957
0.075	558.67	387.52	2.272	1.093
0.10	556.63	416.96	2.256	1.265

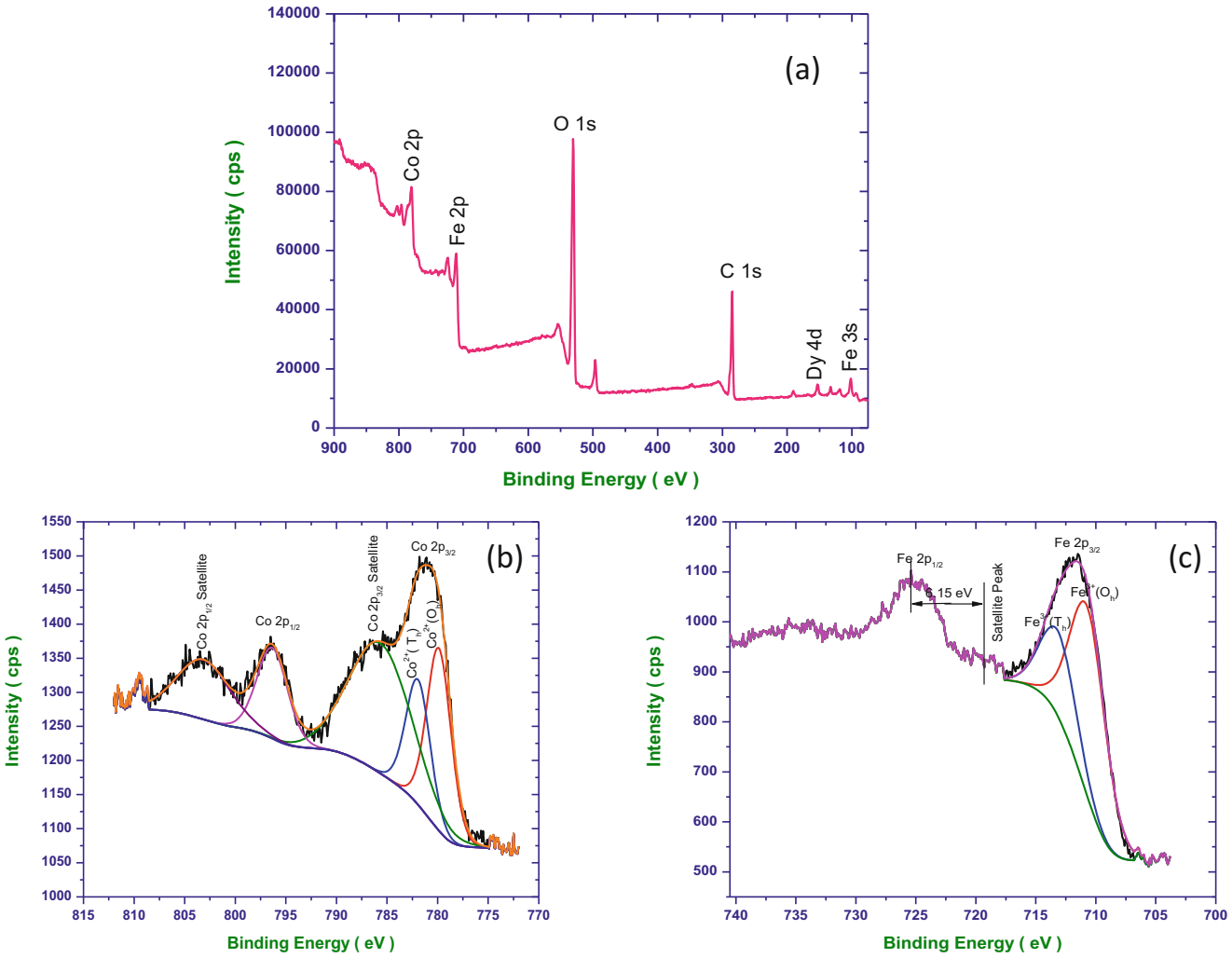

Fig. 5 XPS spectrum (**a**), deconvolution of the Co $2p_{3/2}$ region (**b**), and the Fe $2p_{3/2}$ region (**c**) of $CoFe_{2-x}Dy_xO_4$ ($x = 0.05$) nanoparticles synthesized by starch-assisted sol–gel combustion method

3.6 Magnetic Property

In order to understand the effect of Dy^{3+} in the cobalt ferrite nanoparticles on magnetic properties, magnetization measurements were carried out on a vibrating sample magnetometer at room temperature with a maximum applied field of 10 kOe. The hysteresis loops of the $CoFe_{2-x}Dy_xO_4$ ($x = 0.0, 0.025, 0.05, 0.075, 0.1$) nanoparticles synthesized by starch-assisted sol–gel combustion method are shown in Fig. 6. From the hysteresis loops, the coercive force (H_c), saturation magnetization(M_s), ratio of remanence to saturation magnetization(M_r/M_s) and magnetic moment(η_B) have been calculated and as listed in Table 1. With the increase of dopant content of Dy^{3+}, saturation magnetization (M_s) decreases from the value 13.98 ($x = 0.0$) to 9.66 erg/g ($x = 0.10$). The saturation magnetization value of undoped cobalt ferrite nanoparticles is lower than bulk cobalt ferrite [49]. The decrease in M_S of nanocrystalline undoped cobalt ferrite can be attributed to the surface effect, sometimes called the "dead" surface. The dead surface is associated with disorder of surface spins. The net magnetic moments (η_B) in the ferrimagnetic ferrite materials depend on the number of magnetic ions occupying the tetrahedral and octahedral sites; therefore, the change in the magnetization is dependent on type and number of magnetic ions at different sites. It was found by XPS study that the relative contributions of the Co^{2+} ions at the octahedral and tetrahedral sites were 60 and 41 %, respectively, in the $CoFe_{2-x}Dy_xO_4$ ($x = 0.05$) nanoparticles synthesized by starch-assisted sol–gel combustion method, while the distribution of Fe^{3+} ions was about 69 % at the octahedral sites and about 31 % at the tetrahedral sites. The magnetic moment per formula unit, according to Neel's two sublattice model is given by the difference of magnetic moment of each sublattice [50].

$$M = M_B - M_A$$

where M_B and M_A are the B and A sublattice magnetic moments in μ_B, respectively.

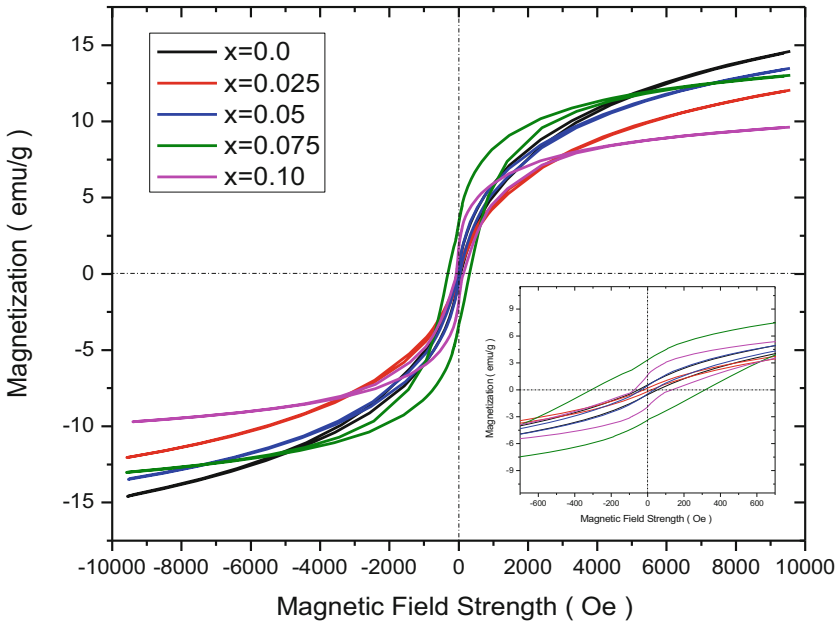

Fig. 6 The magnetic hysteresis loop of $CoFe_{2-x}Dy_xO_4$ (x = 0.0, 0.025, 0.05, 0.075, 0.1) nanoparticles synthesized by starch-assisted sol–gel auto-combustion method. Enlarge view of hysteresis curve is shown as *inset*

It is well known that AB_2O_4 spinel crystal structure consist of intersublattice (A–B) superexchange interactions and intrasublattice (A–A) and (B–B) exchange interactions. Intersublattice superexchange interactions of the cations on the (A–B) are much stronger than on the (A–A) and (B–B) intrasublattice exchange interactions [51]. Generally, Dy^{3+} ions occupy the octahedral sites in the ferrite which causes Co^{2+} ions to migrate from the B site to the A site. This occupancy of Dy^{3+} and Co^{2+} ions changes the difference of magnetic moment between A and B sublattice which resulted in the change in magnetic properties. The dependence of the magnetic moment per formula unit in Bohr magneton (η_B) on the Dy^{3+} dopant concentration in cobalt ferrite nanoparticles, as shown in Table 1, was calculated by using the following relation [52]:

$$\eta_B = (M \times M_s)/5585$$

where M is the molecular weight of a particular ferrite composition and M_s is saturation magnetization (emu/g).

Z. Karimi et al. [53] also observed decrease in saturation magnetization, and it was related to the replacement of Co^{2+} by Dy^{3+} in the cobalt ferrite lattice. It is believed that due to the weakening of A–B exchange interaction, decrease in the saturation magnetization occurred [54, 55]. There will be a dependence of anisotropy constant K on the Dy^{3+} ion concentration x, as listed in Table 1, which is evaluated by using the following relation [52]:

$$H_c = 0.96\ K/M_s$$

where K is an anisotropy constant.

Table 1 shows the variation of coercivity with Dy^{3+} substitution. From Table 1, it can be observed that with the increase of dopant content, coercivity (H_c) first decreases from the value 52.38 Oe ($x = 0.0$) to 21.29 Oe ($x = 0.025$), and then rises up to 312.84 Oe ($x = 0.075$), and finally decreases to 103.46 Oe ($x = 0.10$). The dependence of the coercivity with Dy^{3+} substitution can be correlated with the variation of grain size, and it is a known fact that coercivity is inversely proportional to the grain size. Larger grain tends to contain a more number of domain walls. The magnetization or demagnetization caused by domain wall movement requires less energy than that required by domain rotation. On contrast with the contribution to magnetization or demagnetization due to domain rotation, the wall movement increases as the number of walls increases with increasing grain sizes. Therefore, the $CoFe_{2-x}Dy_xO_4$ ($x = 0.025$) nanoparticles having larger grains are expected to have lower coercivity, as compared with the $CoFe_{2-x}Dy_xO_4$ ($x = 0.00$) nanoparticles. Furthermore, increase in coercivity of $CoFe_{2-x}Dy_xO_4$ nanoparticles with increase of grain size and Dy^{3+} dopant content was observed and it was 312.84 Oe for $x = 0.075$. With increase of dopant content and grain size, impurity or foreign phase $DyFeO_3$ starts to play the role in influencing the coercivity of ferrite. In reported literature [56, 57], impurities distributed in the grain boundary area break and go against the displacement of domain walls. Due to the existence of the foreign phase $DyFeO_3$, the samples after doping with more Dy^{3+} ions were expected to have larger coercivity.

4 Conclusion

The influence of Dy^{3+} substitution on the structural and magnetic properties of the $CoFe_{2-x}Dy_xO_4$ (x = 0.00 to 0.1 in step of 0.025) nanoparticles synthesized by

starch-assisted sol–gel auto-combustion method were investigated. XRD pattern revealed the formation of cubic spinel ferrite with the signature of $DyFeO_3$ phases for $x \geq 0.05$. The field emission scanning electron microscopy study demonstrated the spherical nanoparticle in the size range 5−15 nm. Raman spectroscopy study indicated the change in the octahedral and tetrahedral site-related Raman modes in the Dy^{3+} ion-doped cobalt ferrite nanoparticles. An infrared spectroscopy study showed the presence of two absorption bands in the frequency range around 560 cm^{-1} (ν_1) and around 380 cm^{-1} (ν_2), which indicate the presence of the tetrahedral and octahedral group complexes, respectively, within the spinel ferrite nanoparticles. The X-ray photoelectron spectroscopy (XPS) analysis confirmed the presence of Co^{2+} at the octahedral as well as the tetrahedral site in the $CoFe_{2-x}Dy_xO_4$ ($x = 0.05$) nanoparticles. Room temperature magnetization characterizations showed that the saturation magnetization and coercivity changes with Dy^{3+} addition. It was observed that rare earth ions dopant, grain size, foreign phase $DyFeO_3$ affect the magnetic properties of cobalt ferrite nanoparticles.

Acknowledgments This work was supported by Project Excellent Teams - CZ.1.07/2.3.00/30.0005 and CZ.1.07/2.3.00/30.0039 at Materials Research Centre, Brno University of Technology and project Centre of Polymer Systems (reg. number CZ.1.05/2.1.00/03.0111) at Tomas Bata University in Zlin, Czech Republic.

References

1. Dong-Hyun, K., David, E.N., Duane, T.J., Christopher, S.B.: J. Magn. Magn. Mater. **320**, 2390 (2008)
2. Ngo, A.T., Pileni, M.P.: J. Phys. Chem. B **105**, 53 (2001)
3. Sousa, M.H., Tourinbo, F.A.: J. Phys. Chem. B **105**, 168 (2001)
4. Han, D.H., Luo, H.L., Yang, Z.: J. Magn. Magn. Mater. **161**, 376 (1996)
5. Valenzuela, R.: Magnetic Ceramics. Cambridge University Press (1994)
6. Myrtil, L., Kahn, Z., Zhang, J.: Appl. Phys. Lett. **78**, 3651–3654 (2001)
7. Panda, R.N., Shih, J.C., Chin, T.S.: J. Magn. Magn. Mater. **257**, 79–86 (2003)
8. Muthuselvam, I.P., Bhowmik, R.N.: J. Magn. Magn. Mater. **322**, 767–776 (2010)
9. Tahar, L.B., Smiri, L.S., Artus, M., Joudrier, A.L., Herbst, F., Vaulay, M.J., Ammar, S., Fievet, F.: Mater. Res. Bull. **42**, 1888–1896 (2007)
10. Zhao, L., Cui, Y., Yang, H., Yu, L., Jin, W., Feng, S.: Mater. Lett. **60**, 104–108 (2006)
11. Kumar, L., Kar, M.: Cer. Int. **38**, 4771–4782 (2012)
12. Kim, C.S., Yi, Y.S., Park, K.-T., Namgung, H., Lee, J.-G.: J. Appl. Phys. **85**, 5223–5225 (1999)
13. Hutlova, A., Niznansky, D., Rehspringer, J.-L., Estourn es, C., Kurmoo, M.: Adv. Mater. **15**, 1622–1625 (2003)
14. Pillai, V., Shah, D.O.: J. Magn. Magn. Mater. **163**, 243–248 (1996)
15. Shafi, K.V.P.M., Gedanken, A., Prozorov, R., Balogh, J.: Chem. Mater. **10**, 3445–3450 (1998)
16. Kim, Y.I., Kim, D., Lee, C.S.: Phys. B **337**, 42–51 (2003)
17. Mumtaz, A., Maaz, K., Janjua, B., Hasanain, S.K., Bertino, M.F., Magn, J.: Magn. Mater. **313**, 266–272 (2007)
18. Seip, C.T., Carpenter, E.E., O'Connor, C.J., John, V.T., Li, S.: IEEE Trans. Magn. **34**, 1111–1113 (1998)
19. Cote, L.J., Teja, A.S., Wilkinson, A.P., Zhang, Z.J.: Fluid Phase Equilibr. **210**, 307–317 (2003)
20. Mallikarjuna, N.N., Lagashetty, A., Venkataraman, A.: J. Therm. Anal. Calorim. **74**, 819–826 (2003)
21. Karimi, Z., Mohammadifar, Y., Shokrollahi, H., Khameneh Asl, Sh., Yousefi, Gh., Karimi, L.: J. Magn. Magn. Mater. **361**, 150–156 (2014)
22. Kambale, R.C., Song, K.M., Won, C.J., Lee, K.D., Hur, N.: J. Cryst. Growth **340**, 171–174 (2012)
23. Kambale, R.C., Song, K.M., Koo, Y.S., Hur, N.: J. Appl. Phys. **110**, 053910 (2011)
24. Patil, S.A., Otari, S.M., Mahajan, V.C., Patil, M.G., Patil, A.B., Soudagar, M.K., Patil, B.L., Sawant, S.R.: Solid State Comm. **78**, 39 (1991)
25. Sileo, E.E., Rotelo, R., Jacobo, S.E.: Phys. B **320**, 257 (2002)
26. Jacobo, S.E., Fano, W.G., Razzitte, A.C.: Phys. B **320**, 261 (2002)
27. Sileo, E.E., Jacobo, S.E.: Phys. B **354**, 241 (2004)
28. Ramalho, M.A.F., Gama, L., Antonio, S.G., Paiva-Santos, C.O., Miola, E.J., Kiminami, R.H.G.A., Costa, A.C.F.M.: J. Mater. Sci. **42**, 3603 (2007)
29. Duong, G.V., Turtelli, R.S., Hanh, N., Linh, D.V., Reissner, M., Michor, H., Fidler, J., Wiesinger, G., Grossinger, R.: J. Magn. Magn. Mater. **307**, 313–317 (2006)
30. Wang, Z., Lazor, P., Saxena, S.K., O'Neill, H.S.C.: Mater. Res. Bull. **37**(9), 1589–1602 (2002)
31. Chandramohan, P., Srinivasan, M.P., Velmurugan, S., Narasimhan, S.V.: J. Solid State Chem. **184**, 89–96 (2011)
32. Cvejic, Z., Rakic, S., Kremenovic, A., Antic, B., Jovalekic, C., Colomban, P.: Solid State Sci. **8**, 908 (2006)
33. Urcia-Romero, S., Perales-Pérez, O., Gutiérrez, G.: J. Appl. Phys. **107**, 09A508 (2010)
34. Shemer, G., Tirosh, E., Livneh, T., Markovich, G.: J. Phys. Chem. C **111**, 14334–14338 (2007)
35. Liu, W., Chan, Y., Cai, J., Leung, C., Mak, C., Wong, K., Zhang, F., Wu, X., Qi, X.D.: J. Appl. Phys. **112**, 104306 (2012)
36. Zhao, X., Wang, W., Zhang, Y., Wu, S., Li, F., Liu, J.P.: Chem. Eng. J. **250**, 164–174 (2014)
37. Waldron, R.D.: Infrared Spectra of Ferrites. Phys. Rev. **99**, 1727 (1955)
38. Labde, B.K., Sable, M.C., Shamkuwar, N.R.: Mater. Lett. **57**, 1651–1655 (2003)
39. Gabal, M.A., AlAngari, Y.M., Zaki, H.M., Magn, J.: Magn. Mater. **363**, 6–12 (2014)
40. Raut, A.V., Barkule, R.S., Shengule, D.R., Jadhav, K.M., Magn, J.: Magn. Mater. **358-359**, 87–92 (2014)
41. Cheng, F.X., Jia, J.T., Xu, Z.G., Zhou, B., Liao, C.S., Yan, C.H., Chen, L.Y., Zhao, H.B.: J. Appl. Phys. **86**, 2727 (1999)
42. Cheng, F.X., Liao, C., Kuang, J., Xu, Z., Yan, C., Chen, L., Zhao, H., Liu, Z.: J. Appl. Phys. **85**, 2782 (1999)
43. Zaki, H.M., Dawoud, H.A.: Phys. B **405**, 4476 (2010)
44. Shirsath, S.E., Kadam, R.H., Mane, M.L., Ghasemi, A., Yasukawa, Y., Liu, X., Morisako, A.: J. Alloys Compnd. **575**, 145–151 (2013)
45. Srinivasan, T.T., Srivastava, C.M., Venkatramni, N., Patani, M.J.: Bull. Mater. Sci. **5**, 1063 (1984)
46. Jaffari, G.H., Lin, H.Y., Ni, C., Shah, S.I.: Mater. Sci. Eng. B **164**, 23–29 (2009)

47. Tholkappiyan, R., Vishista, K.: Physica B (2014). doi:10.1016/j.physb.2014.04.022
48. Wang, W.P., Yang, H., Xian, T., Jiang, J.L.: Mater. Trans. **53**(9), 1586–1589 (2012)
49. Sodaee, T., Ghasemi, A., Paimozd, E., Paesano, A. Jr., Morisako, A.: J Magn. Magn. Mater. **330**, 169–173 (2013)
50. Neel, L.: Ann. Phys. Paris **3**, 137–198 (1948)
51. Pachpinde, A.M., Langade, M.M., Lohar, K.S., Patange, S.M., Shi, S.E.: Chem. Phys. **429**, 20–26 (2014)
52. Kambale, R.C., Shaikh, P.A., Kamble, S.S., Kolekar, Y.D.: J. Alloys Comp. **478**, 599 (2009)
53. Karimi, Z., Mohammadifar, Y., Shokrollahi, H., Khameneh Asl, S., Yousefi, Gh., Karimi, L.: J. Magn. Magn. Mater. **361**, 150–156 (2014)
54. Kambale, R., Song, K., Won, C., Lee, K., Hur, N.: J. Cryst. Growth **340**, 171–174 (2011)
55. Ali, I., Islam, M., Ishaque, M.: J. Magn. Magn. Mater **324**, 3777 (2012)
56. Pachpinde, A.M., Langade, M.M., Lohar, K.S., Patange, S.M., Shirsath, S.E.: Chem. Phys. **429**, 20–26 (2014)
57. Peng, Z., Fu, X., Ge, H., Fu, Z., Wang, C., Qi, L., Miao, H.: J. Magn. Magn. Mater. **323**, 2513 (2011)